JOURNAL OF GEOPHYSICAL RESEARCH, VOL. 90, NO. C3, PAGES 4756–4772, MAY 20, 1985

Drifter Observations of Coastal Surface Currents During CODE: The Statistical and Dynamical Views

RUSS E. DAVIS

Scripps Institution of Oceanography, La Jolla, California

Observations of near-surface coastal currents were made off the Northern California coast during CODE by using 164 current-following drifters. These observations are used to describe the two-dimensional structure of the mean surface flow and the scales of its variability. The mean flow is a broad equatorward current, strongly sheared only within 10 km of the shore, and a mean offshore flow producing an average divergence $\nabla_H \cdot \mathbf{u} \approx 3 \times 10^{-6}\,s^{-1}$. Divergence is uniformly distributed across the shelf, but variation of the alongshore flow causes an upwelling center near Point Arena. The spatial correlation scale is less than 40 km in both the alongshore and across-shelf directions, even though 55% of the surface kinetic energy is described by a single mode with gradual across-shelf variation and an alongshore wavelength of the order 200 km. The surface flow is well correlated with flow at 30-m depth. The Lagrangian time scale ($\approx$1.5 day) is significantly shorter than the Eulerian time scale ($\approx$5 days), indicating that the flow is dominated by highly nonlinear quasi-stationary eddies. Drifter displacements indicate that the mean lateral eddy transport of passive scalars can be described by an anisotropic and inhomogeneous eddy diffusivity, but this diffusivity cannot be used to relate eddy Reynolds stresses and the mean shear. Analysis of two-particle separations, which determine the size of dispersing property clouds, shows that dispersal cannot be described by a scale-dependent diffusivity and indicates the importance of small-scale convergences in retarding dispersal. Over the entire 100-km by 50-km region the surface layer heat budget is dominated by upwelling cooling and surface heating, with onshore eddy heat flux playing a smaller role. Substantial convergence of the alongshore eddy heat flux is apparently required to balance upwelling cooling in the upwelling center. Drifters are found to have a Lagrangian mean acceleration caused by eddy processes. Analysis of this acceleration and of the horizontal flow contributions to the eddy Reynolds stress allows examination of the importance of eddy processes in the mean momentum budget. While the alongshore flow must be in approximate geostrophic balance, there is a clear pattern to the eddy forcing, which appears to be important in the alongshore momentum equation.

1. INTRODUCTION

In a companion paper, *Davis* [this issue, hereafter called part 1], the current-following drifter subprogram of the Coastal Dynamics Experiment (CODE) was described. One objective of that program was description of the spatial patterns of near-surface flow, including the effects of bathymetric and coastline features. Motivated by the *Bryden et al.* [1980] exploration into the role of eddy fluxes in the coastal heat budget, another objective was description of eddy transport, including determination of the flow features that support eddy fluxes. In part 1 the observational technique was described, and examples of various flow features, such as jets, eddies, convergences, and vigorous across-shelf "squirts," were shown. The complexity of individual examples precludes assimilation of the entire data set and makes it difficult to separate typical and unusual events.

In order to describe the typical rather than individual examples and to determine the dynamical consequences of mesoscale features disclosed by these examples, this paper presents a number of statistical and dynamical analyses. Section 2 describes offshore profiles of mean velocity and eddy Reynolds stress, Lagrangian and Eulerian time scales, spatial scales of velocity variability, and the most energetic modes of current variability. Lagrangian analyses in section 3 lead to description of lateral mixing of the mean field as determined by single-particle dispersion and lateral stirring of individual property clouds as determined by two-particle dispersion. In section 4, objective maps of mean velocity, Reynolds stress, and mean Lagrangian acceleration are used to discuss the mean heat and momentum balances. A synopsis of the results is given in section 5.

1.1 *The Data*

The CODE region, its bathymetry, and the location of the various moored current observations are shown in Figure 1. Comparisons with moored current observations in this paper are limited to results from moorings C3, C4, C5, M3, and R3 during 1981; these data are summarized by *Winant and Bratkovich* [1980]. Drifter observations were taken during May and July of 1981 and 1982. During this season, the CODE region has the highest mean, upwelling-favorable wind stress found along the West Coast [*Nelson*, 1977].

A total of 133 surface drifters were deployed (approximately half in each year) along with 31 drifters drogued at 30-m depth in 1982. The record lengths and sampling frequency from different buoys vary. There were 1177 surface drifter and 360 drogue fixes taken; these gave 670 and 195 buoy-days of data, respectively. Velocities were

Copyright 1985 by the American Geophsical Union.

Paper number 4C1355.
0148-0227/85/004C-1355$05.00

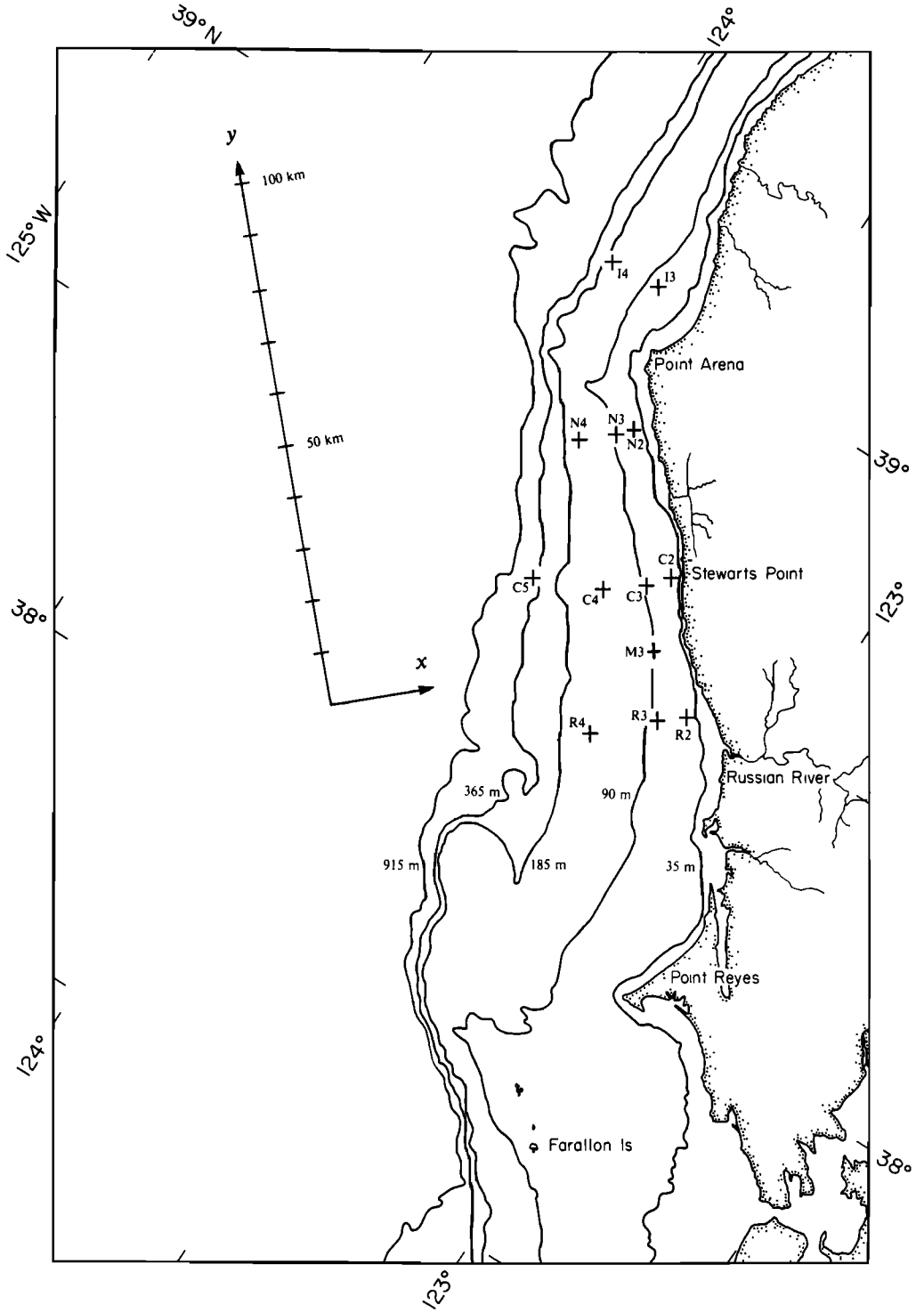

Fig. 1. The CODE region and bathymetry. San Francisco Bay is 40 km south of Point Reyes. The locations of current meter moorings from 1981 and 1982 are indicated. The upcoast and onshore directions y and x are also shown.

computed from fix pairs separated by 0.6 to 1.2 days, yielding 720 observations of 1-m currents and 217 observations of 30-m currents from nonoverlapping time intervals. For Eulerian averaging, each velocity observation was given the position and time midway between the two associated fixes. In discussion, directions and velocity components are referenced to axes aligned with 317°T, as shown in Figure 1. "Alongshore," "upcoast," y, and v refer to 317°T, while "across-shelf," "onshore," x, and u refer to 47°.

Typically, 8 to 15 drifters were set along one to three offshore lines within 20 km of the coast; a majority of these lines were between Point Arena and Stewarts Point. The density of observations varies geographically. A typical rectangle with $\Delta x = 10$ km and $\Delta y = 20$ km located within 40 km of the coast between Point Arena and the

Russian River contains 35 surface and 12 30-m velocity observations. Similar rectangles outside this region, but within 60 km of the coast in the CODE region, contain half as many observations.

1.2 *Averaging and Bias*

Here, typical conditions are described by time averages. Both Eulerian and Lagrangian averages are employed. The terms "Eulerian velocity" and "Lagrangian velocity" are sometimes erroneously used to distinguish these averages; actually, there is only one velocity field, and coordinate frames are important only in describing what is held constant during averaging. Eulerian means ($<\cdot>_E$) include all observations in a specified geographical region. Lagrangian means ($<\cdot>_L$) are over observations made following all drifters "deployed" in a region. Actually, it is assumed that drifters found at $\mathbf{x}_o$ have the same statistics as drifters deployed at $\mathbf{x}_o$. This assumption, which is only strictly true in horizontally nondivergent flows [*Davis*, 1983], allows one drifter to be used in several Lagrangian ensembles.

Eulerian averages represent the typical state at a point. To provide unbiased Eulerian averages, observations at a point must be randomly or uniformly spaced in time. It is important that velocity observations are made along Lagrangian paths only if the probability of an observation being made at a point depends on the velocity there. Thus the initial velocity of randomly deployed drifters provides an unbiased Eulerian average. But because the velocity being averaged also determines the the sampling array, there are three basic ways that drifter-based Eulerian velocity statistics can be biased.

The most obvious cause of bias in drifter-derived Eulerian statistics is an intrinsic correlation between particle position and velocity such as produces Stokes Drift of particles on a wave-disturbed surface. Part of Stokes Drift reflects the fact that the average surface velocity at a point differs from the average at a fixed level. Convergence of the surface flow, which concentrates particles in regions of high velocity, produces additional drift. A similar effect produces drift of constant level floats in most flows that are not horizontally nondivergent [*Davis*, 1982]. The comparisons in part 1 and the theoretical calculations [cf. *Kenyon*, 1969] indicate that, in CODE, Stokes Drift bias is less than 3 cm/s and is alongshore, the direction of wave propagation. The effect of frontal convergences can not be estimated.

Large scale variation of drifter density also affects the bias of Eulerian averages. Drifters were deployed primarily in the northern part of the CODE region, so most observations in the south are made following southward flow; this might be expected to produce a bias. Fortuitously, the correlation time of drifter velocity is so short that a drifter's history, which determines its location, is poorly correlated with its present velocity; thus this bias is not believed significant in the CODE analysis.

The third cause of bias in drifter-derived Eulerian averages is inhomogeneity of the small-scale, eddy-dispersive velocity field. Particles released from a point in a zero-mean velocity field with spatially variable eddy energy will drift toward high eddy energy [cf. *Freeland et al.*, 1975]. Similarly, particles will migrate away from a boundary where dispersion is prevented. *Davis* [1983] analyzes the paradox that particles placed at a point have a different mean velocity than those passing through that point. Basically, in the ensemble of particles released at $\mathbf{x}$ the particles moving toward high energy have larger average speeds than those moving toward low energy. In the ensemble passing through $\mathbf{x}$ this effect is balanced by the tendency for particles coming to $\mathbf{x}$ from high energy regions to have the higher speed. In CODE, bias of this sort is most serious near the shore, but as discussed in section 3.1, it is negligible even there.

Drifters are, of course, subject to instrumental errors like windage; these are included in the 3-cm/s error bound. Only a perfect surface drifter moves vertically like a true Lagrangian particle, so drifters must be regarded as quasi-Lagrangian. This quasi-Lagrangian nature is not a problem for Eulerian statistics, since drifters provide velocity observations at a prescribed level. While in some cases the separation of drifter and Lagrangian particles will become significant with time, this is important to the Lagrangian statistics here only if that separation is typically comparable with the particle displacements or particle-pair separations considered. By this measure the errors from internal wave scale motions are insignificant, but the effects of frontal convergences are impossible to estimate. It is, therefore, necessary to bear in mind that if there are large vertical velocities in fronts in the CODE region then the drifter statistics reported here may differ from true particle statistics.

2. SCALES OF VARIATION

2.1 *Profiles of Mean Velocity and Reynolds Stress*

Across-shelf profiles of mean horizontal surface velocity $<\mathbf{u}(\xi)>_E$ are shown in Figure 2. These were computed

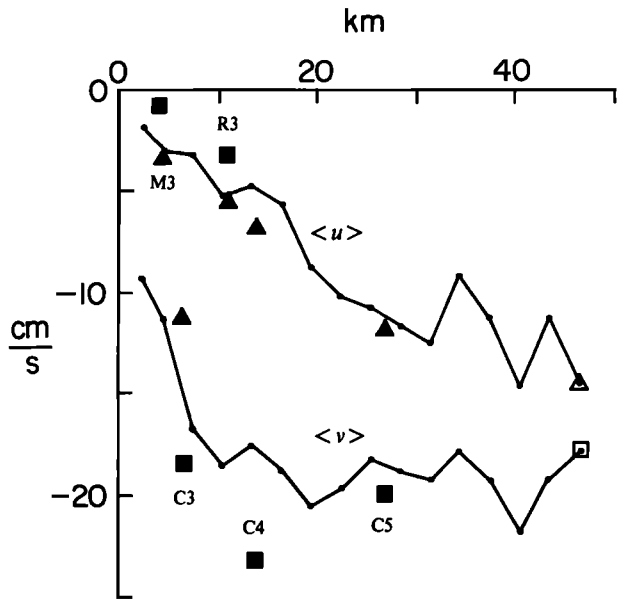

Fig. 2. Mean upcoast near-surface velocity $<v>_E$ (squares) and onshore velocity $<u>_E$ (triangles) as a function of offshore distance. Solid symbols are 1981 averages from shallow current meters on the moorings indicated. Note the divergence $\partial_x <u>$ and the decrease of downcoast flow near the coast.

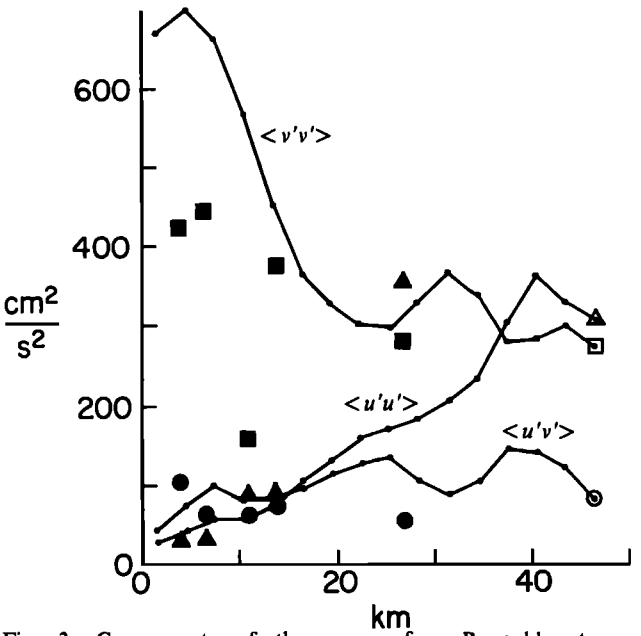

Fig. 3. Components of the near-surface Reynolds stresses $\langle v'v' \rangle_E$ (squares), $\langle u'u' \rangle_E$ (triangles), and $\langle u'v' \rangle_E$ (circles) versus offshore distance. Fluctuations are based on the mean values of Figure 2. Solid symbols are from 1981 current meters. Note how $\langle u'^2 \rangle$ and $\langle v'^2 \rangle$ vary oppositely and become isotropic offshore.

by averaging observations in 3-km bins of offshore distance ξ (defined as the shortest distance between the coast and the observation) and then smoothing with a 1-2-1 filter. Velocity fluctuations $\mathbf{u}'$ were defined by using $\langle \mathbf{u}(\xi) \rangle_E$, and the eddy Reynolds stress $\langle \mathbf{u}'\mathbf{u}' \rangle_E$ was computed by using the averaging procedure above; the results are shown in Figure 3. The statistical reliability of these results depends on the number of observations averaged and their correlation. From the scale information presented below it is estimated that the averages involve 40 to 100 degrees of freedom.

For comparison, statistics from near-surface current meters are included in Figures 2 and 3; these were computed from 1-day averages (roughly comparable to the time span of drifter-derived velocities) from the 90-day period encompassing the 1981 drifter deployments. The current meters used were at 4-m depth on mooring C3 (see Figure 1 for mooring locations), 19-m on C4, and 9-m on C5, M3, and R3; the statistics involve approximately 30 effective degrees of freedom.

The mean offshore velocity increases approximately linearly with offshore distance from near zero at the coast to 12 cm/s at $\xi = 40$ km, implying an average surface divergence of $3 \times 10^{-6}\,s^{-1}$. The mean downcoast flow is near 20 cm/s for $\xi > 10$ km but approaches zero at the coast, inducing a nearshore shear of the order $10^{-5}\,s^{-1}$. The variance of across-shelf velocity increases approximately linearly with ξ from near zero at the coast, while the alongshore variance is largest near shore. The opposite trends of $\langle v'^2 \rangle$ and $\langle u'^2 \rangle$ lead to approximate isotropy near $\xi = 35$ km and a total kinetic energy that varies little with ξ.

Comparison of drifter and current meter means is reasonable. Offshore flow at mooring C3, where there is significant vertically integrated offshore transport, is anomalously large, and the alongshore flow at R3 and C3 also differ widely. The suggestion from current meters that alongshore flow is weaker to the south is confirmed by the drifter-based maps of section 4. There are two reasons to believe that the small values of $\langle v \rangle_E$ obtained from nearshore drifters are not the result of sampling bias: (1) a majority of samples in the nearshore averages are from recently deployed drifters whose locations are, therefore, not yet biased by the flow; (2) current meters on the 30- and 60-m isobaths on the C line also show weak alongshore flow. Similarly, as discussed in section 3.1, the drifter estimates of $\langle u \rangle_E$ are not significantly biased because the gradient of diffusivity is small and the density of drifter observations does not vary much across the shelf. It is believed that the discrepancy between current meter and drifter values of nearshore $\langle v'^2 \rangle$ reflects the spatial variation of time-averaged currents which appear as variations to the drifter analysis.

The $3 \times 10^{-6}\,s^{-1}$ divergence implied by the profile of $\langle u \rangle$ varies less with offshore distance than would be supposed if wind-driven upwelling were confined to the inner shelf; the implications of surface divergence to the mean mass and heat budgets are discussed in section 4.2. The profile of $\langle v \rangle$ shows little evidence of the surface jet found in synoptic observations off Oregon by *Mooers et al.* [1976]. Rather, the appearance is that of a broad current that is markedly sheared only over the inner shelf. If a jet existed, but varied its offshore distance with time or alongshore position, it would be smoothed out in our average picture. The dynamics of the mean surface flow are discussed in section 4.3.

The principle axis of the Reynolds stress obtained by averaging together all offshore distances is 337°T compared with the upcoast direction 317°. This indicates that typical downcoast current events are associated with offshore flow, as one might expect for wind forcing.

2.2 *Time Scales*

Lagrangian time-lagged velocity correlations were computed by averaging time-lagged velocity products from individual drifters. Observations were segregated into 0.5-day bins of time lag and by offshore distance. The Lagrangian mean time-lagged correlation of the principal components of the Reynolds stress, $\hat{v}$ and $\hat{u}$, are shown in Figure 4. For the curves labeled $\xi < 20$ km, at least one of the two velocity observations was less than 20 km offshore; all other observation pairs are included in the $\xi > 20$ km curves. For comparison the Eulerian averaged, time-lagged velocity correlations derived from 1-day means of the 9-m current meters at M3 ($\xi = 5$ km) and C5 ($\xi = 27$ km) are shown in Figure 5. Correlations from current meters vary little with instrument depth . The correlations from R3 closely resemble those shown for M3; the $\hat{u}$ correlations from C3 resemble the M3/R3 results, but the time scale of $\hat{v}$ is much shorter, about the same as the scale of $\hat{u}$.

Ninety-day record means were used in computing the velocity correlations from current meters. In computing the Lagrangian averages it was necessary to treat the Lagrangian mean velocity $\langle \mathbf{u}(\mathbf{x}_o, t) \rangle_L$ as a function of t, the time since deployment. This very interesting

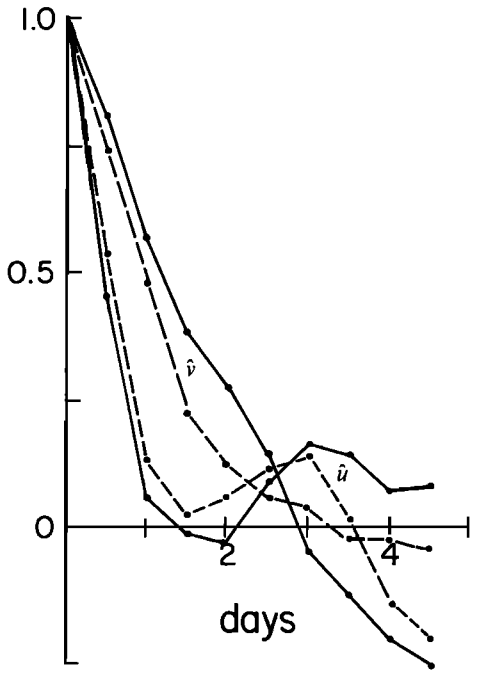

Fig. 4. Lagrangian time-lagged correlation of principal components of velocity from surface drifters. Solid curves are for drifters within 20 km of the coast; dashed curves are for offshore drifters.

Lagrangian mean acceleration is discussed in section 4.3; it is neither an instrument error nor an indication of Eulerian nonstationarity but rather an indication of eddy forcing in the mean momentum equation.

The most striking feature in Figures 4 and 5 is that the Lagrangian time scale is much smaller than the Eulerian scale. This is equally true of the energy-containing eddy time scales (such as the e-folding time) and the temporal microscale computed from mean square acceleration (or the second derivative of the velocity correlation at zero lag). This is to be contrasted with the results of *Freeland et al.* [1975], who found, for mid-depth mesoscale eddies, that the Eulerian and Lagrangian energy-containing eddy time scales were comparable but that the Eulerian microscale was significantly smaller than its Lagrangian analogue. These authors suggested that the shorter Eulerian microscale should be a general result; the CODE results and the theoretical results of *Davis* [1982, 1983] show this not to be the case.

Comparison of the Eulerian time scale τ_E and the Lagrangian scale τ_L is an important descriptor of the nonlinear processes occurring in the flow field. If the flow is weak enough that the nonlinear terms in the field acceleration $\partial_t \mathbf{u} + \mathbf{u} \cdot \nabla \mathbf{u}$ can be neglected, then $\tau_E \approx \tau_L$; this is clearly not the case in CODE. If the field consists of a slowly varying large scale flow in which small eddies are advected as frozen features (as supposed in Taylor's hypothesis), then the energy-containing eddy scales will be comparable, but the Eulerian microscale will be shorter than the Lagrangian microscale; this describes the results of *Freeland et al.* [1975] but is not the case in CODE. If the flow consists of a field of vigorous eddies in which the fluid velocity is much greater than the eddy propagation velocity, then $\tau_E >> \tau_L$ because material particles see rapid changes as they sweep through the effectively stationary eddies. This is the case in CODE and, in fact, inspection of individual buoy array tracks discloses many examples of buoys sweeping through complex, but essentially stationary, flow patterns.

Examination of Figures 4 and 5 shows that the time scale of the principal component $\hat{v}$ exceeds that of $\hat{u}$ for both Eulerian and Lagrangian averaging and that time scales, like energy levels, become isotropic offshore.

2.3 *Spatial Scales*

Although the CODE surface velocity field is clearly neither statistically isotropic nor homogeneous, a crude picture of its horizontal scales of variability is provided by the correlation of simultaneous velocity observations as a function of separation distance. This correlation was computed from all 1981 and 1982 observation pairs separated by less than 0.5 day by using separation bins of 5-km width and the alongshore-averaged mean velocities in Figure 2. The results, shown in Figure 6, show a remarkably short correlation distance of the order 40 km, indicating that the complex structures seen in part 1 are not atypical. The alongshore component has somewhat longer scales than the across-shelf component.

Also shown in Figure 6 are cross correlations between surface drifter and 30-m drogues. Nearby surface and 30-m velocities are highly correlated, and the shape of the surface versus surface and surface versus 30-m correlations do not differ significantly. This demonstrates that a majority of the features observed by drifters are not superficial and extend over at least the upper 30-m.

In order to gain a true picture of the spatial structure of typical surface current variability features it is necessary to

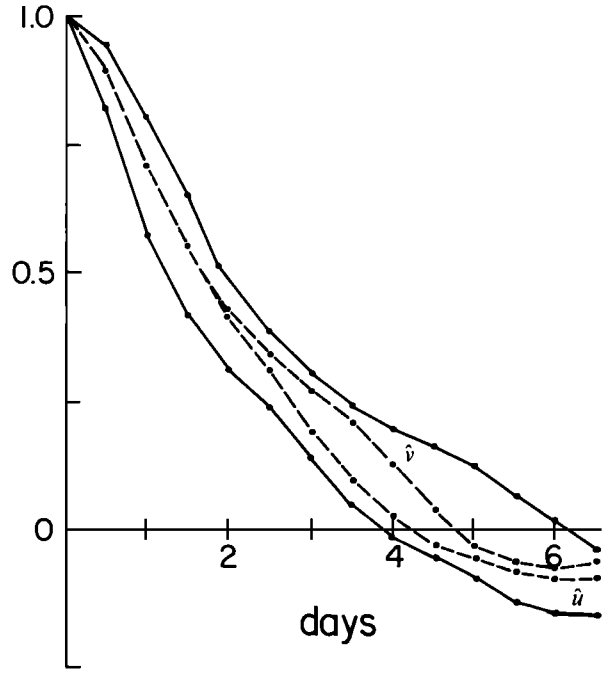

Fig. 5. Time lagged correlation of principal components of velocity from shallow current meters. Solid curves are from nearshore 1981 mooring M3; dashed curves are for offshore mooring C5. Note that the Eulerian time scale is greater than the Lagrangian time scale (Figure 4).

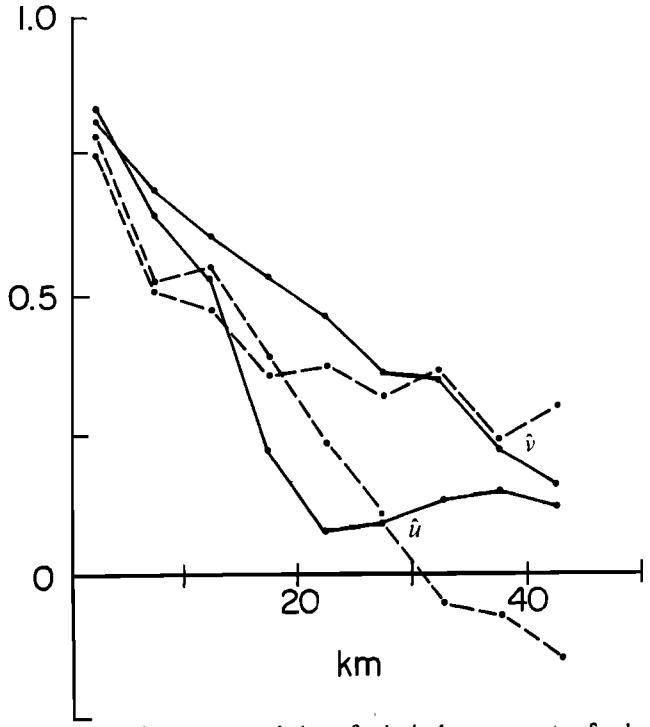

Fig. 6. Simultaneous correlation of principal components of velocity as a function of distance between observations. Solid curves are correlations between surface drifters, dashed curves are surface drifters with 30-m drogues. The latter shows that effects observed at the surface are typical of the upper layer.

account for anisotropy and across-shelf inhomogeneity. This can be done by considering x and y variations separately and by using two-point (x_1 and x_2) statistics rather than lag ($x_1 - x_2$) statistics, in the across-shelf direction. Because this requires averaging over narrowly defined categories, for which there are few observations, it is possible to draw statistically significant results only by sacrificing temporal and spatial resolution. Thus the signal of interest was taken to be those velocity fluctuations passing a 3-day, 20-km (alongshore) by 10-km (across-shelf) rectangular low-pass filter. The covariance of this filtered velocity was estimated from the very unequally spaced drifter observations by using the method described in the Appendix.

For discussion, the covariance of filtered velocity at ξ_1, y_1, t and at ξ_2, y_2, t is taken as $\tilde{C}(\xi_1, \xi_2, y_1 - y_2)$. Figure 7 shows the correlation of filtered velocities at fixed offshore distance as a function of their alongshore separation; the curves plotted are based on averages of $\tilde{C}[\xi, \xi, y]$ over the ranges $0 < \xi < 15$ km and $30 < \xi < 45$ km. Figure 8 shows the correlation of velocities at fixed alongshore position as a function of their across-shelf separation; the plotted curves are based on averaging $\tilde{C}[\xi, x+\xi, 0]$ over 15-km ranges of ξ centered on $x = 7.5$ km and $x = 37.5$ km. Also plotted in Figures 7 and 8 are the analogous correlations of 3-day averaged velocity from the current meters listed in section 2.1. The current meter correlations are scattered, indicating either small scale inhomogeneity of statistics or limited statistical reliability. Because of this scatter, it can only be said that the current meter and drifter results are not inconsistent.

Figure 7 shows that the y scales of both u and v are longest near shore, with v better correlated than u; the scales of u and v are similar offshore. Figure 8 shows the across-shelf scale of u to vary little with offshore distance. The x scale of v is largest near shore, exceeding that of u, but offshore the scale of v decreases significantly. Correlations decrease smoothly with alongshore separation y, but variation with x is irregular. It is remarkable that currents separated by 50 km in the alongshore direction are effectively uncorrelated, even near shore. This emphasizes the importance of the complex flow structures seen in the examples of part 1 and shows that near-surface coastal currents vary significantly over alongshore distances less than the scales of the wind and the major variations of bathymetry.

The most compact description of the spatial structure of variability is obtained by decomposing the filtered velocity covariance dyad into its vector eigenfunctions (empirical orthogonal functions) according to

$$\tilde{C}(\xi_1, \xi_2, y) = \sum_n \langle a_n(y_o, t_o)\, a_n(y_o + y, t_o) \rangle \mathbf{U}_n(\xi_1)\mathbf{U}_n(\xi_2)$$

where the empirical modes $\mathbf{U}(\xi)$ are orthonormal when summed over ξ from 2.5 to 42.5 km in 5-km steps. This representation has the property that each mode contributes to the summed kinetic energy

$$\sum_\xi \langle \mathbf{u}'(\xi) \cdot \mathbf{u}'(\xi) \rangle$$

in proportion to the associated $\langle a_n^2 \rangle$ and that the N modes with the largest $\langle a_n^2 \rangle$ explain more of the variance than any other N member family of functions. Figures 9 and 10 depict the u and v components of the two

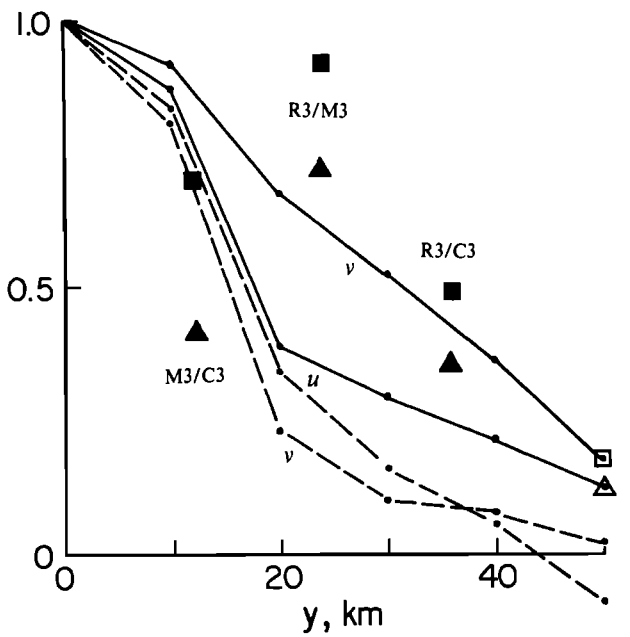

Fig. 7. Alongshore lagged correlations of the velocity components v (squares) and u (triangles) from surface drifters and 1981 near-surface current meters. Solid curves are for offshore distances less than 15 km; dashed curves are for 30 to 45 km offshore distance. Solid symbols are from mooring pairs indicated. Note that nearshore v has a long length scale; offshore the scales u and v are similar.

modes that explain the largest fraction of the variance; also shown are the alongshore correlations of the associated mode amplitudes $a_n(y)$.

The dominant mode, shown in Figure 9, explains a surprising 55% of the variance. The v component is maximum at the coast and decreases without change of sign out to an offshore distance of 45 km; the u component increases uniformly with offshore distance from a value near zero at the coast. In this mode, downcoast flow is associated with offshore flow, much as one would expect for wind-driven currents in which offshore Ekman flow and downcoast currents result from downcoast winds. The alongshore scale of the dominant mode is long, suggesting a typical wavelength of the order 200 km or more.

The second mode, depicted in Figure 10, explains 18% of the variance. The u component increases with offshore distance from zero at the coast, much like the first mode. Alongshore velocity reverses with offshore distance; upcoast flow nearshore (and downcoast flow offshore) accompany offshore velocities. The individual examples with the most significant across-shelf shear of v are nearshore current reversals that follow wind relaxation events; the second mode structure suggests that such reversals also involve offshore flow and surface current divergence!

While 73% of the surface kinetic energy is described by two relatively simple modes, the interference of these and other less energetic modes, plus those components removed by space-time filtering, lead to relatively short correlation scales of the order 40 km. This gives the experimentalist some warning about the difficulty of verifying models of large-scale variability from point measurements. Detection of the large-scale components of flow will require considerable spatial filtering.

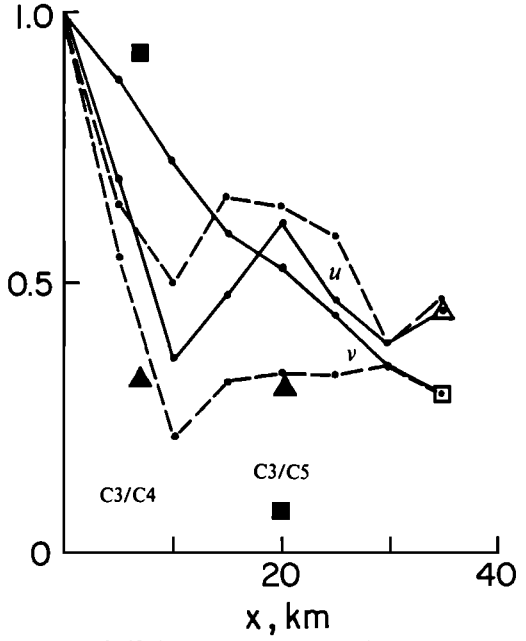

Fig. 8. Across-shelf lagged correlation of the velocity components v (squares) and u (triangles) from surface drifters and 1981 near-surface current meters. Solid curves are correlated with a point 7.5 km offshore; dashed curves are correlated with a point 37.5 km offshore. Solid symbols are from mooring pairs indicated. Note that the scales of u do not change much with offshore distance. Near shore the scale of v exceeds the u scale, whereas offshore the v scale is shorter.

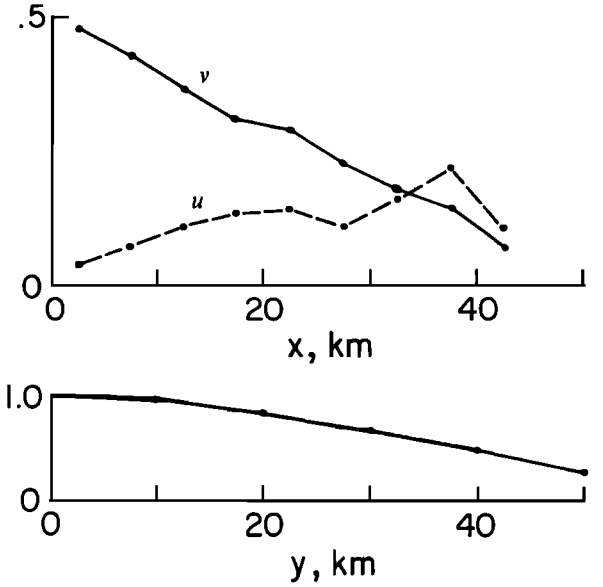

Fig. 9. The principal empirical mode, which explains 55% of the surface current variance. The upper panel shows the vector components *vs.* offshore distance. The lower panel is the alongshore correlation of this mode's amplitude. The finite correlations at large scale in Figures 7 and 8 result primarily from this mode, whose alongshore scale exceeds the size of the CODE region.

3. LAGRANGIAN ANALYSIS OF TRANSPORT PROCESSES

The Lagrangian nature of the CODE drifters may be exploited to characterize "eddy diffusive" lateral transport. Single particle dispersion determines diffusive transport in the mean distribution of scalar properties. Particle-pair statistics describe the typical size of individual dispersing property "clouds" and also disclose the importance of small scale convergences.

3.1 *Single-Particle Dispersion*

The mean concentration of a scalar property is determined by its initial distribution, sources and sinks, and the probability density of particle displacement that is the Green's Function of the mean concentration evolution equation [cf. *Davis*, 1983]. If $\mathbf{r}(\mathbf{x},t)$ is the position of a particle originating from $\mathbf{x}$ at $t=0$, then simple measures of the probability density are the mean displacement and the covariance

$$\mu_{nm}(\mathbf{x},t) = \langle r'_n(\mathbf{x},t) r'_m(\mathbf{x},t) \rangle .$$

Figure 11 depicts μ computed from all CODE surface drifters by using a mean displacement field obtained by objectively fitting [*Davis*, 1984] to a constant plus terms linear in x and y. The displacement covariance of 30-m drogues does not differ significantly from Figure 11, as might have been anticipated from the results of section 2.3.

If mean scalar transport were described by a linear flux-gradient law with slowly varying diffusivity κ, and the effects of shear and boundaries were negligible, then $\mu(t)$ would be a linear function of t with

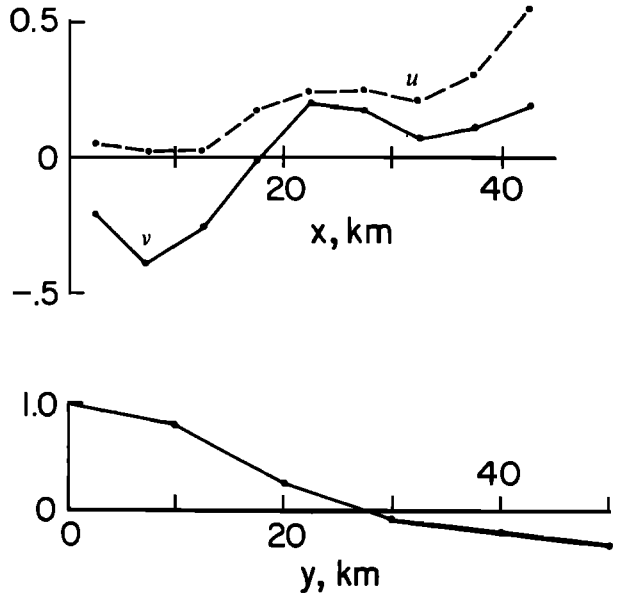

Fig. 10. As Figure 9 for the second mode, which explains 17% of the variance.

$$\kappa(\mathbf{x}) = \frac{1}{2}\frac{d}{dt}\mu(\mathbf{x},t)\,. \tag{1}$$

The observed temporal variation of μ is essentially linear, reflecting the short Lagrangian time scale found in section 2.2.

In order to assess effects of shear and inhomogeneity, the apparent diffusivity $\tilde{\kappa}(\mathbf{x})$ was defined from (1) as the average of $\frac{1}{2}\frac{d}{dt}\mu(\mathbf{x},t)$ from $t = 0.5$ day to 2.5 days. There was no detectable variation of $\tilde{\kappa}(\mathbf{x})$ with alongshore position nor any spatial dependence of the small cross-term $\tilde{\kappa}_{xy}$. The significant dependence of $\tilde{\kappa}_{xx}$ and $\tilde{\kappa}_{yy}$ on ξ was found to be well modeled by

$$\tilde{\kappa}_{yy}(\xi) = 3.5\times 10^7 \frac{\text{cm}^2}{\text{s}} - \xi\cdot 4\frac{\text{cm}}{\text{s}}, \quad \tilde{\kappa}_{xx}(\xi) = \xi\cdot 3\frac{\text{cm}}{\text{s}}$$

Following the pattern of velocity variance, across-shelf dispersion increases offshore from a value near zero at the coast, while alongshore dispersion is greatest at the coast. As with energy levels, time scales, and space scales, dispersion becomes more isotropic with offshore distance, and isotropy is achieved about 50 km offshore.

Histograms of particle displacement show that the probability density is not exactly of the Gaussian form required for a zero-shear gradient-diffusion model. The skewness of alongshore displacement,

$$S_y(t) = \langle r'_y{}^3(t)\rangle / \langle r'_y{}^2(t)\rangle^{3/2}$$

consistently falls in the range 0.4—0.5 for all t and $\mathbf{x}_o$. Thus most drifters move downcoast faster than the mean velocity, but there are more extreme displacements upcoast than down. The skewness of across-shelf displacement for drifters originating more than 20 km offshore is a reasonably constant $S_x \approx -0.3$; the skewness for drifters originating within 20 km of the coast varies from $S_x \approx -1.0$ at $t = 1$ day to $S_x \approx -0.7$ after 3 days. These skewnesses indicate that, as might be anticipated, anomalously large displacements are more often offshore than onshore.

The alongshore dispersion results are reasonably consistent with a mean flux versus gradient law with true diffusivity κ_{yy} equal to $\tilde{\kappa}_{yy}$. Alongshore dispersion is not affected by the coastline, and the larger nearshore $\tilde{\kappa}_{yy}$ reflects a larger true diffusivity. In fact, offshore variation is well described by $\kappa_{yy}(\xi) = \langle v'^2(\xi)\rangle\tau$, where $\langle v'^2\rangle$ is taken from Figure 3 and $\tau \approx 5\times 10^4$ s is approximately the integral time scale obtained from Figure 4. Inspection of the individual examples included in the alongshore displacement statistics indicates that the anomalously large displacements causing skewness often come from relatively nearshore drifters caught in the infrequent but large upcoast flows following wind relaxation events. Thus the observed skewness may be a reflection of truly non-Gaussian velocity statistics or an effect of the nearshore shear of $\langle v\rangle$ seen in Figure 2.

Interpretation of the observed across-shelf dispersion is complicated by the dependence of $\langle u\rangle_E$ and $\tilde{\kappa}_{xx}$ on offshore distance. An appropriate model with which to test the idea that dispersion obeys a gradient diffusion law with diffusivity κ_{xx} is

$$\partial_t C + \partial_x \langle u\rangle C = \partial_x \kappa_{xx}\partial_x C\,, \tag{2}$$

where $x = 0$ at the shore, $\langle u\rangle = U'x$, $\kappa_{xx} = \kappa' x$, and $C(x,t)dx$ is the probability that a particle will be found between x and $x+dx$ at time t and is analogous to the concentration of a scalar property. Moments of particle position, $r(t)$, can be obtained by noting that

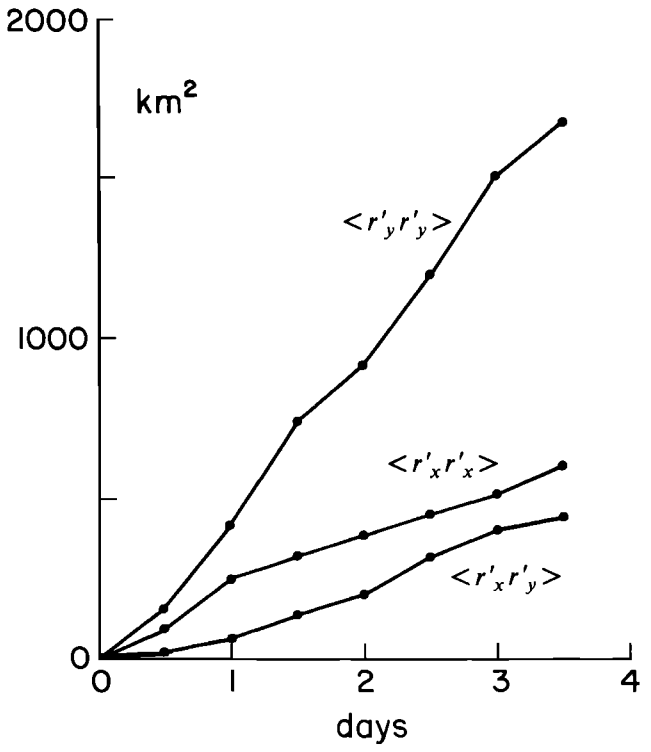

Fig. 11. The components of the covariance of particle displacement μ as a function of time. These curves are based on all CODE surface drifters. The single-particle diffusivity, proportional to the curves' slopes, is relatively constant.

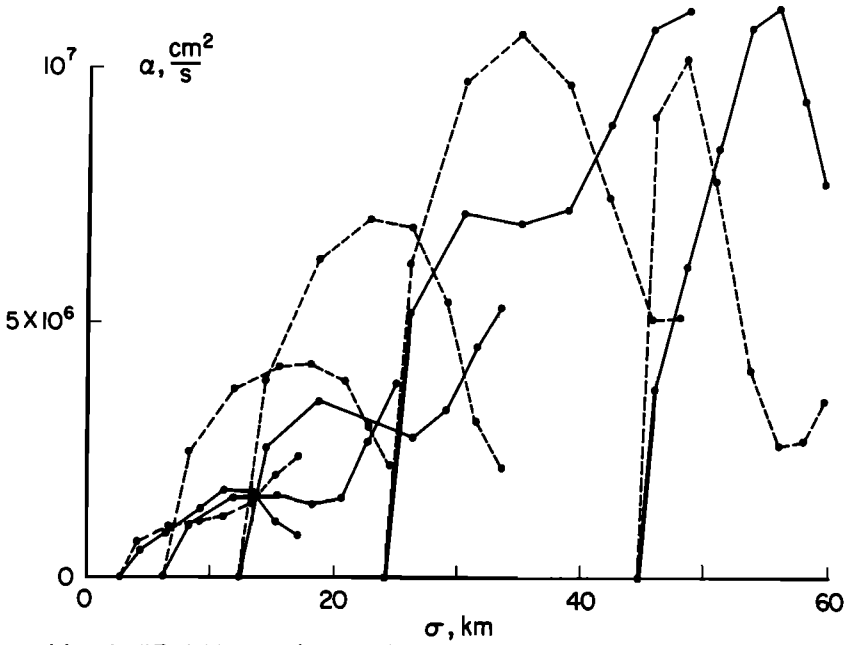

Fig. 12. The particle-pair diffusivities $\alpha_{\hat{x}\hat{x}}$ (solid line) and $\alpha_{\hat{y}\hat{y}}$ (dashed) as a function of root mean square separation σ for various initial separations s_0. Both α and σ depend on time, and a point is plotted every half day. The point where $\alpha = 0$ corresponds to $t = 0$ and $\sigma = s_0$, allowing $\alpha(t)$ and $\sigma(t)$ to be found by counting plotted points. A simple α versus σ relation is not found because α depends on both σ and t; note how each component of α has its own characteristic time dependence. Thus two-particle dispersion is not well described by a scale-dependent diffusivity.

$$\frac{d}{dt}<r^n> = \int_0^\infty dx\, x^n\, \partial_t C(x,t)\,,$$

substituting (2) and integrating by parts. This leads to

$$\frac{d}{dt}<r^n> = nU'<r^n> + n^2\kappa'<r^{n-1}>\,. \qquad (3)$$

from which moments of r are easily found.

Calculations with (3), using values of $U' = 4\times 10^{-6}\,s^{-1}$ (from Figure 2) and κ' in the range 0.5–3 cm/s, indicate that the inhomogeneity of κ_{xx} and the offshore increase of $<u>$ conspire to make the apparent diffusivity, $\tilde{\kappa}_{xx}$, significantly larger than the true diffusivity and to introduce negative skewness. Close agreement between predicted and observed $\tilde{\kappa}_{xx}$ was obtained with $\kappa_{xx}(\xi) = \xi \cdot 0.8$ cm/s. The advection-diffusion model with this κ_{xx} does not, however, explain the observed temporal variation of the skewness S_x. For $\xi_o \approx 10$ km the predicted skewness varies from $S_x \approx -0.5$ after 1 day to -0.8 after 3 days; over the same period the observed skewness varies oppositely from -1.0 to -0.7. For $\xi_o \approx 30$ km the model predicts S_x to grow from -0.2 at 1 day to -0.4 after 3, perhaps reasonable agreement with the observed $S_x \approx -0.3$.

Are the estimates of Eulerian mean velocity biased by the variation of κ_{xx} or the presence of a coastline? The Lagrangian mean velocity $<u>_L$ of particles released at a single point differs from $<u>_E$ by $\partial_x\kappa_{xx}$, here an offshore bias of less than 1 cm/s. But the bias of $<u>_E$ estimated by averaging over all particles passing through a region is very much less and would vanish if the overall density of drifters were uniform. Similarly, the bias that might be introduced by the inhibiting influence of the coastline is negligible because κ_{xx} is very small near the coast.

In summary, Lagrangian analysis of single particle statistics indicates that there is little sampling bias of estimated Eulerian mean velocity and that eddy transport in the long-term mean budget of a passive scalar may be approximately described by a flux versus gradient law with eddy diffusivity

$$\kappa_{xx} = \xi \cdot 0.8\frac{cm}{s}, \quad \kappa_{xy} = 0.8\times 10^7\frac{cm^2}{s}$$
$$\kappa_{yy} = 3.5\times 10^7\frac{cm^2}{s} - \xi \cdot 4\frac{cm}{s}, \qquad (4)$$

The analogy with gradient diffusion does not exactly describe the observed skewness of particle concentration, but this discrepancy would not have significant impact in most modeling situations.

A model relating the mean eddy flux of a scalar to an eddy diffusivity is not necessarily phenomenological; the probability density of particle displacement is the Green's Function of the mean transport equation, and if its evolution is described by a diffusivity (as it is here), then so is the mean field's evolution. But to relate the transport of momentum by eddy stresses to particle dispersal requires another assumption about how a particle's velocity changes. It is, therefore, not surprising that the observed Reynolds stresses are not related to the mean shear using κ as an eddy viscosity. For example, the alongshore mean shear stress $-\rho<u'v'>$ is not related to the mean shear $\partial_x<v>$ by $-<u'v'> = \kappa_{xx}\partial_x<v>$. The largest value of $\kappa_{xx}\partial_x<v>$ obtained from the diffusivity in (4) and the

mean shear in Figure 2 is found at an offshore distance of the order 10 km, where $\kappa_{xx} \approx 10^6 \text{cm}^2/\text{s}$ and $\partial_x \langle v \rangle \approx -10^{-5}\text{s}^{-1}$. If κ were used as an eddy viscosity, these would predict a $\langle u'v' \rangle$ of the order $10\text{cm}^2/\text{s}^2$, whereas the observed value from Figure 3 is near $50\text{cm}^2/\text{s}^2$. Farther offshore the comparison is even worse because the increase of κ_{xx} is more than balanced by the reduction of $\partial_x \langle v \rangle$ so that the predicted stress decreases while the observed stress increases. Thus it must be concluded that the use of κ as an eddy viscosity leads to Reynolds stress estimates that are in error by a varying factor of the order 10.

3.2 *Particle-Pair Dispersion*

While single-particle statistics determine eddy transport of the mean field, multiparticle statistics are required to describe the typical stirring of individual property fields. The typical growth of a property cloud's size is determined by particle-pair separation statistics [cf. *Csanady*, 1973; *Davis*, 1983]. If the time and space scales of velocity are sufficiently short, then mean field transport can be modeled as diffusion. But for the typical stirring of individual clouds to be described by gradient diffusion, the mean square separation between particles must increase linearly with time and the vector components of separation must be normally distributed. This rarely occurs because the typical relative velocity between particles increases as their separation increases. Thus mean square separation usually increases more rapidly than linearly in time; *Garrett* [1983] indicates an initially exponential increase for closely spaced particles in two-dimensional turbulence. An early approach to particle-pair dispersion was use of "scale-dependent" diffusivities [*Richardson*, 1926].

If $\mathbf{r}(\mathbf{x},t)$ is the position of a particle starting from $\mathbf{x}$ at time $t=0$, then $\mathbf{s}(t,\mathbf{s}_o,\mathbf{c}) = \mathbf{r}(t,\mathbf{c}+\mathbf{s}_o/2) - \mathbf{r}(t,\mathbf{c}-\mathbf{s}_o/2)$ is the separation vector (with initial value $\mathbf{s}_o$) of a particle pair having initial center position $\mathbf{c}$. By analogy with particles in a diffusive medium, a particle-pair diffusivity may be defined as

$$\alpha_{nm}(t,\mathbf{s}_o,\mathbf{c}) = \frac{1}{4}\frac{d}{dt}\langle s_n'(t,\mathbf{s}_o,\mathbf{c}) s_m'(t,\mathbf{s}_o,\mathbf{c}) \rangle$$

where the average is over many pairs with the same starting locations. In a truly diffusive medium without mean shear, α would be constant and equal to the single-particle diffusivity κ. Because the value of α is proportional to the covariance of $\mathbf{s}'$ and the relative velocity between the particles, it is initially zero for particles placed randomly in real flows. After sufficient time, particles become widely separated, their motions become independent, and α approaches κ.

Analysis of separation statistics in CODE is complicated by the anisotropy and inhomogeneity of the velocity field; this makes α depend on both the vectors $\mathbf{s}_o$ and $\mathbf{c}$. The larger the number of parameters influencing separation statistics the more resolution must be sacrificed to obtain statistical reliability. Therefore, the first analysis objective was to find those variables having little effect on low order moments of $\mathbf{s}$. Separation statistics did not appear to depend on the orientation of the initial separation $\mathbf{s}_o$ or on the alongshore component of position, $\mathbf{c}$, and rotation to the principal axes of the Reynolds stress (335°T, see section 2.2) reduced correlations of $s'_{\hat{x}}$ and $s'_{\hat{y}}$ to insignificant values. Thus exploration was limited to autostatistics of $s_{\hat{x}}$ and $s_{\hat{y}}$ and their dependence on t, $s_o = |\mathbf{s}_o|$ and initial offshore distance, $c_{\hat{x}}$.

The pair diffusivity $\alpha(t,s_o)$ was computed from all simultaneous surface drifter records. Records of particle separation were segregated into logarithmically spaced bins of initial separation s_o, the mean square separation $\sigma^2(t,s_o)$ was computed, and the diffusivity was calculated from 1-day differences. Between 30 and 100 days of record were used in each s_o bin. The integral time scale of relative velocity varies from near 0.5 day (for particles separated by about 10 km) to 1.5 days (for separations of the order 50 km). The ratio of record length to integral time scale exaggerates the effective number of samples in the average because the velocity field has a finite correlation length, making different particle pairs statistically dependent. Comparing results from various halves of the data set indicates that the diffusivity estimates are reliable to about 30%.

Figure 12 shows the pair diffusivity α plotted as a function of the Rms separation σ; the t dependence of α can be determined from that figure by using the points plotted every half day. Figure 12 shows little evidence of the initially exponential growth of α predicted by *Garrett* [1983]. This prediction is based on the assumption that the diffusivity depends primarily on particle separation, and a very rough α versus σ relation can be seen in Figure 12. As expected, this rough relation shows α to increase with σ for small separations and shows little increase for the range $\sigma > 30$ km in which α is of the same order as the single particle diffusivity κ; this is consistent with the 40 km velocity decorrelation length found in Figure 6. The pair diffusivity increases with σ because both the variance and integral time scale of the relative velocity between particles increases. Both α_{xx} and α_{yy} increase about 50% as $c_{\hat{x}}$ increases from 10 to 50 km; recall that the single-particle diffusivity κ_{yy} decreases with offshore distance.

While Figure 12 shows a rough α versus σ dependence, the relationship is scattered because α depends on both σ and t; that the scatter in the α versus σ relation is not statistical noise can be seen by the characteristic temporal evolution of α seen in the curves for each s_o range. As *Batchelor* [1952] was apparently the first to note, one does not expect *Richardson*'s [1926] hypothesis that pair diffusivity depends primarily on typical separation to pertain in detail, and in fact, *Davis*' [1983] simulations of particle motion in random velocity fields show the same kind of complex α versus σ and t curves found in Figure 12. While it is likely that the CODE velocity field differs significantly from the two-dimensional turbulence *Garrett* [1983] was addressing, it is clear that no theory that depends on a simple α versus σ relation will lead to the complex structures in Figure 12, and it must be suspected that such theories simply do not apply to many real situations.

The diffusivity α describes the variance of separation $\mathbf{s}(t,\mathbf{s}_o)$, but a complete description of particle-pair statistics requires knowledge of the full probability density of $\mathbf{s}$. The probability distribution of $s = |\mathbf{s}|$ discloses some interesting features of the CODE velocity field that would

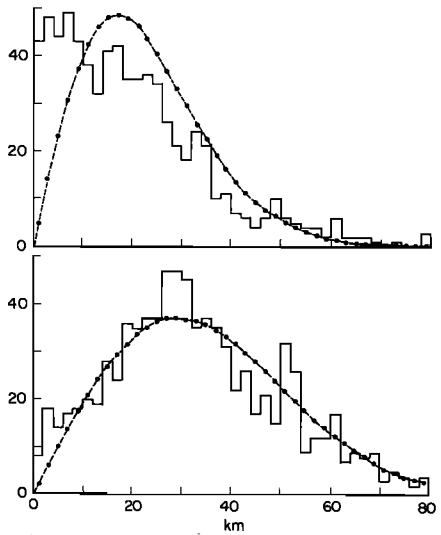

Fig. 13. Histograms of particle-pair separation after 4 days for initial separation in the ranges $4 < s_o < 16$ km (upper curve) and $16 < s_o < 30$ km (lower curve). The solid bar plot shows the number of pairs falling within the associated 2 km range of separation. The dashed lines indicate the values expected if separation, s, were normally distributed. Note the excess number of small separation observations for the $s_o < 16$ km case.

have been difficult to detect by any other means. Figure 13 shows the histogram of s after 4 days for initial separations in the ranges $4 < s_o < 16$ km and $16 < s_o < 30$ km. Also shown are the values one would expect if s were normally distributed with mean $\mathbf{s}_o$ and the observed variance distributed equally between the two components. This was obtained by convolving the theoretical probability density

$$f(s, s_o) = \frac{1}{\pi <q^2>} s\, e^{-(s-s_o)^2/<q^2>} \int_0^{2\pi} d\theta\, e^{2ss_o[\cos(\theta)-1]/<q^2>}$$

with the number of pairs initially in various 2-km subranges of s_o.

The striking observation in Figure 13 is that the Gaussian-s model describes the separation distribution for large s_o, but the observed distribution for small s_o contains many more small separations than the model predicts. This may be evidence of small scale velocity convergences in which closely spaced particles can be trapped, or it may result from the explosive exponential growth of separation between particles in a large scale shear field. Figure 6 of part 1 shows an example of convergence trapping, and the histogram in Figure 13 includes many other, more sporadic, examples.

Additional description of the motion of particle pairs is provided by moments of

$$\mathbf{q}(t, \mathbf{s}_o) = \mathbf{s}(t, \mathbf{s}_o) - \mathbf{s}_o .$$

Since the major inhomogeneity in the CODE region is offshore variation, the particle pairs used to define separation were ordered so that the $\hat{x}$ component of initial separation $\mathbf{s}_o$ was always positive. In a diffusive medium with vanishing mean shear, $\mathbf{q}$ would be normally distributed with zero mean. The following observations summarize the moments of $\mathbf{q}$:

1) For all $\mathbf{s}_o$ and t the mean of $\mathbf{q}$ is negligible. This is surprising in light of the significant divergence $\partial_x <u>_E \approx 3 \times 10^{-6} s^{-1}$ found in section 2.1; a $<q_{\hat{x}}>$ increasing at this rate should have been detected.

2) For all $\mathbf{s}_o$ and t, $<q_{\hat{y}}^3> \approx 0$ and $<q_{\hat{x}}^3> \approx 0.5 <q_{\hat{x}}^2>^{3/2}$. This skewness indicates that the extreme changes of separation are amplifications of the initial separation rather than cases where the offshore particle order is reversed.

3) For all $\mathbf{s}_o$ and t the kurtoses $<q_{\hat{x}}^4>/<q_{\hat{x}}^2>^2$ and $<q_{\hat{y}}^4>/<q_{\hat{y}}^2>^2$ are approximately equal. For $s_o > 15$ km and $t > 1$ day, kurtoses were found near 4 (little bigger than the 3 expected for Gaussian variables). But for $\mathbf{s}_o < 10$ km and times of the order 1 day, values of the order 10 were found; this indicates that, as seen in Figure 13, the relative motion of closely spaced particles is intermittent.

4. Structure and Dynamics of the Mean Field

Drifters provide spatially extensive sampling from which maps of Eulerian average fields are easily constructed. By exploiting the Lagrangian nature of drifters, additional quantities of dynamical interest, such as the nonlinear field acceleration terms in the momentum budget and rates of eddy transport, can be observed directly. In this section these capabilities are exploited to examine the mean budgets of mass, heat, and momentum in the CODE region. The principal results are based on two-dimensional maps of average quantities such as Eulerian mean surface velocity, Reynolds stress, and Lagrangian mean acceleration.

4.1. *Mapping*

Three methods of mapping mean fields from the irregular drifter sampling array were explored: (1) direct averaging over spatial bins, (2) minimum mean square error estimation (objective mapping), and (3) objective function fitting. The results from these methods are similar, but each has characteristics peculiar to the method employed. Averaging over spatial bins produces maps with significant interbin noise unless additional smoothing is applied. Applying spatial filters to bin averages involves determining how to weight different bins that have differing statistical sampling errors; this appears to require introduction of some statistical measure of error such as used in the other two methods. Objective mapping [*Bretherton et al.*, 1976] seeks the map with minimum expected square error and, consequently, involves statistical descriptions of both the signal and noise. The results of section 2 serve to adequately characterize the noise (here temporal variability), but the "statistics" of the signal (here the mean field) are hard to define, let alone determine. Even if one defines expectation values with respect to a Bayesian ensemble of "similar worlds," it is impossible to specify the implied statistics of time-averaged quantities. Nevertheless, if such statistics are hypothesized to have sensible scales, the resulting objective maps are credible in the sense that they agree with the results of the other methods, and with objective maps made from similar hypothesized statistics, to within the expected mapping error. From a methodological point of view, however, the most satisfactory mapping method is objective function fitting, which makes use of

the minimum expected square error criterion but requires specification of only the noise statistics.

The maps presented here are based on objective function fitting. This method, described in *Davis* [1985], is a blend of least square fitting and objective analysis. It involves fitting to a prescribed set of functions by using an expected square error (rather than square misfit) criterion. The mapping error and resolution depend on the number of basis functions employed, and this number can be selected objectively. Deviations from the alongshore averaged profiles of Figures 2 and 3 were fit to polynomials of offshore distance ξ and alongshore position y; use of such deviations minimizes bias from rapid changes of alongshore averages with ξ near the coast. The results shown here are based on third-degree polynomials of ξ and y minus the y^3 and ξy^2 terms (thus eight functions are used). This is judged to be the maximum resolution that can be employed without introducing artifacts of the sampling errors. The noise covariance was specified as stationary, homogeneous, and of an exponential form, with energy and ξ, y, t scales derived from the results of section 2. As noted in section 1.1, the total number of available velocity observations is 720, and their density varies over the region. The features in the maps are believed significant with 90% confidence, i.e., there is 90% probability that eliminating any basis function would lead to a less accurate map.

4.2 *Mean Mass and Heat Budgets*

Figure 14 is the map of mean surface velocity derived from all CODE surface drifters. The large-scale variation with offshore distance in this map could have been deduced from the offshore profiles in Figure 2. The two-dimensional map also shows significant alongshore variation. The flow is predominantly offshore near Point Arena, where the largest divergence, produced primarily by increasing alongshore flow, is found. Flow across the entire shelf seems to be steered offshore as Point Reyes is approached, leading to a deceleration of nearshore flow to the south as inferred from the current meter data in Figure 2. Examination of individual flow examples indicates that the structure near Point Arena is the result of transitory but recurrent "squirts"; the offshore flow at Point Reyes is more nearly a permanent feature. There is a hint of an alongshore jet structure in Figure 14; this was obscured in the across-shelf profile in Figure 2 because the jet's offshore distance changes alongshore.

Divergence, which determines near-surface upwelling, is the surface velocity feature of greatest importance to the mass and heat budgets. The divergence in Figure 14 varies less than 30% with offshore distance at any alongshore location, and there is negligible divergence concentrated at the coast because the normal component of the flow almost vanishes there. This broad scale of divergence is surprising; one might have expected that the mean offshore Ekman transport would be developed within a few kilometers of the coast so that the surface divergence would be concentrated near shore. The area-mean divergence is of the order $3\times 10^{-6}\,s^{-1}$; alongshore variation of $<v>$ makes divergence near Point Arena twice this average, while divergence in the southern region

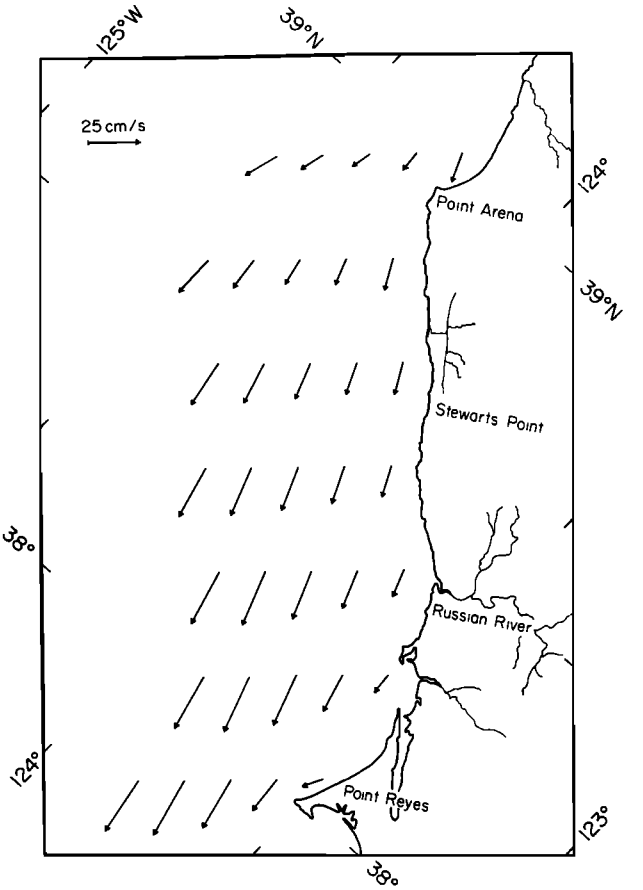

Fig. 14. The mean surface velocity found by objective function fitting. Note the broad across-shelf scale of divergence and the apparent center of divergence near Point Arena.

is somewhat less than average. It is noteworthy that divergence of velocity is about twice the size of the curl (except very near shore, where Figure 2 shows large $\partial_x<v>$).

Surface divergence indicates that there is vertical motion just below the surface, but it does not indicate active upwelling in the sense that deep, cold, nutrient-rich water is being entrained into the surface layer. Surface divergence might be balanced without true upwelling by an offshore reduction of upper-layer thickness. Imagine that the near-surface flow were uniformly distributed over a layer of thickness h with a mean offshore transport of $2\times 10^4\,cm^2/s$, the Ekman transport for the observed [*Beardsley and Mills*, 1982] mean alongshore wind stress of 1.7 dyne cm^{-2} at C3. If the active upwelling occurred near the coast, the observed surface divergence would require the upper layer to shoal offshore from h = 40 m at $\xi = 10$ km to h = 10 m at $\xi = 40$ km. If, on the other hand, $h \approx 20$ m over the entire region, the observed divergence would indicate active upwelling (with an upward velocity of the order 5 m/day below the surface layer) distributed uniformly over the first 40 km offshore. Perhaps examination of mixed layer depths, as disclosed in temperature and salinity profiles, will help determine where active upwelling occurs.

How does the coastal surface layer keep from cooling throughout the spring-summer season when the large equatorward mean wind stress drives an upwelling circula-

tion that continuously exports heat from the shelf region? Clearly, solar insolation balances part of this cooling, but *Bryden et al.* [1980] found onshore eddy heat transport to be important off Oregon, while *Richman and Badan-Dangon* [1983] found convergence of the mean alongshore advective heat flux to be significant off Northwest Africa.

To examine the upper layer heat budget in CODE, it is assumed that temperature is a passive scalar whose mean eddy flux can be computed from the single particle diffusivity κ of section 3.1. This is a bold assumption because part of the eddy heat flux $<\mathbf{u}'T'>$ results from correlation of time-varying Ekman transport and upwelling induced surface temperature fluctuations, a process unlikely to be modeled by gradient diffusion. The flux modeled with κ is more nearly that supported by eddies than the flux from time varying large scale fluctuations. If $(\theta, \mathbf{U})$ denote the mean (temperature, horizontal velocity) and if $\partial_z \mathbf{U}$ and $\partial_{zz}^2 \theta$ are neglected in an upper layer of thickness H, then the upper layer heat budget obtained by integrating vertically from $z=-H$ to $z=0$ is

$$\partial_t \Theta + \mathbf{U}\cdot\nabla\Theta = -\delta_z \nabla\cdot\mathbf{U} + \nabla\cdot\kappa\nabla\Theta + \frac{Q_s - Q_e}{H} \quad (5)$$

where $\Theta = \frac{1}{H}\int_{-H}^{0} \theta\, dz$, $\delta_z = \Theta - \theta(z=-H)$, $\rho c_p Q_s$ is the downward surface heat flux, and $\rho c_p Q_e = -\rho c_p <w'T'>$ is the downward turbulent heat flux at $z=-H$. Thus Θ is the mean layer temperature, δ_z is the temperature difference leading to upwelling cooling, and $Q_s - Q_e$ is the net heating by vertical fluxes. We have no information on Q_e (the analogue of the entrainment flux in models of the well-mixed layer) and only note that its effect is probably to reduce the net heating below the value of Q_s.

In the absence of mean upper layer temperature maps, interest must be restricted to the across-shelf-average heat budget obtained by integrating (5) from $x=-L$ to the coast, $x=0$. Denoting this average by an overbar and using the results in Figures 2 and 14 to justify neglecting $\partial_{xx}^2 u$, this budget is

$$\partial_t \bar{\Theta} + \overline{V\partial_y\Theta} + \overline{\delta_z \partial_y V} - \partial_y \overline{\kappa_{yy}\partial_y\Theta} = \frac{\Delta}{L} u(x=-L) - \frac{1}{L}\kappa_{xx}\frac{\partial\Theta}{\partial x}\bigg|_{x=-L} + \frac{\bar{Q}_s - \bar{Q}_e}{H} \quad (6)$$

where

$$\Delta = \frac{1}{H}\int_{-H}^{0} \theta(-L, z)\, dz - \frac{1}{L}\int_{-L}^{0} \theta(x, -H)\, dx$$

is the average temperature difference between the offshore and lower boundaries of the upper layer control volume. The first term on the right of (6) represents cooling by across-shelf overturning, and the last two terms are the onshore eddy heat flux at $x=-L$ and the net surface heating, respectively.

For typical values from CODE, the right side of (6) represents an approximate balance of upwelling cooling and surface warming, with the across-shelf eddy flux playing a smaller role. For $L \approx 30$ km our results suggest $U(-L) \approx -0.1$ m/s and $\kappa_{xx} \approx 250 m^2/s$. For $H \approx 25$ m, *Huyer*'s [1984] hydrographic sections along the C mooring line give $\delta_z \approx 0.5$°C (more or less uniformly across the section), $\Delta \approx 1.0$°C, and $\partial_x \Theta \approx -5\times 10^{-5}$ °C m^{-1}. R. C. Beardsley (private communication, 1984) reports a mean surface heat flux of 200 W m^{-2}. Neglecting Q_e and any residual $\partial_t \bar{\Theta}$,

$$\overline{V\partial_y\Theta} + \overline{\delta_z\partial_y V} - \partial_y\overline{\kappa_{yy}\partial_y\Theta} = [-3 + 0.5 + 2]\times 10^{-6}\ ^\circ\text{C s}^{-1}$$

where the terms on the right are in the same order as in (6).

In a region like the C mooring line, where $\nabla\cdot\mathbf{U}$ is dominated by $\partial_x U$, upwelling cooling is primarily balanced by surface heating with onshore eddy flux playing a less important role. But near Point Arena, $\partial_y V$ is an important part of the divergence, and the associated upwelling cooling $\overline{\delta_z\partial_y V}$ must be balanced. Since both V and the temperature gradient are to the south, it is unlikely that advection can provide the balance, and it appears that convergence of the alongshore eddy heat flux is required. The divergence of V between Point Arena and the C line induces a cooling ($\approx -2\times 10^{-6}$ °C s^{-1}) to be balanced by convergence of the alongshore eddy heat flux. Since κ_{yy} varies little alongshore, a substantial variation of the alongshore temperature gradient is required to produce this convergence. Thus it is suggested that $\partial_y \bar{V}$ makes the region near Point Arena an "upwelling center" which, it is predicted, will be evidenced by $\partial_{yy}\bar{\Theta} < 0$ and possibly by a local surface temperature minimum.

4.3 *Mean Momentum Budget*

By combining Lagrangian and Eulerian averaging, drifters can be used to examine the effect of eddy stresses on the mean flow. For this it is convenient to separate the velocity field into a small-scale turbulent part plus another larger-scale component with (horizontal, vertical) components $(\mathbf{u}, w)$. The boundary between these components is placed at a spatial scale around 1-m, so that because of their physical size, CODE drifters are not advected by the small scale turbulent component. The mean horizontal momentum equation is then

$$\rho\mathbf{f}\times<\mathbf{u}> + \nabla P - \partial_z\tau = -\rho\nabla\cdot<\mathbf{uu}> - \rho\partial_z<w\mathbf{u}> = -\mathbf{F} \quad (7)$$

where ρ is density, P is mean pressure, and τ is the mean shear stress supported by turbulent components. At the surface, τ equals the mean wind stress. The momentum flux in $\mathbf{F}$ includes contributions from both mean and fluctuating components but not from components smaller than our drifters (≈ 1 m).

As will be seen below, the two terms in the momentum flux $\mathbf{F}$ are of comparable magnitude and, as can be estimated from Figures 2 and 3, are smaller than the mean Coriolis force $\rho\mathbf{f}\times<\mathbf{u}>$ by nearly an order of magnitude. Thus, as expected, the first-order momentum balance involves Coriolis acceleration, wind forcing through τ, and pressure gradients. If this is so, what causes the marked nearshore shear of alongshore flow $\partial_x<v>$, seen in Figure 2? The change of $f<v>$ across the inner 10 km is of the order 10^{-3} cm/s^2 across the inner shelf. For this to be balanced by wind forcing would require $\partial_z\tau_x$ to

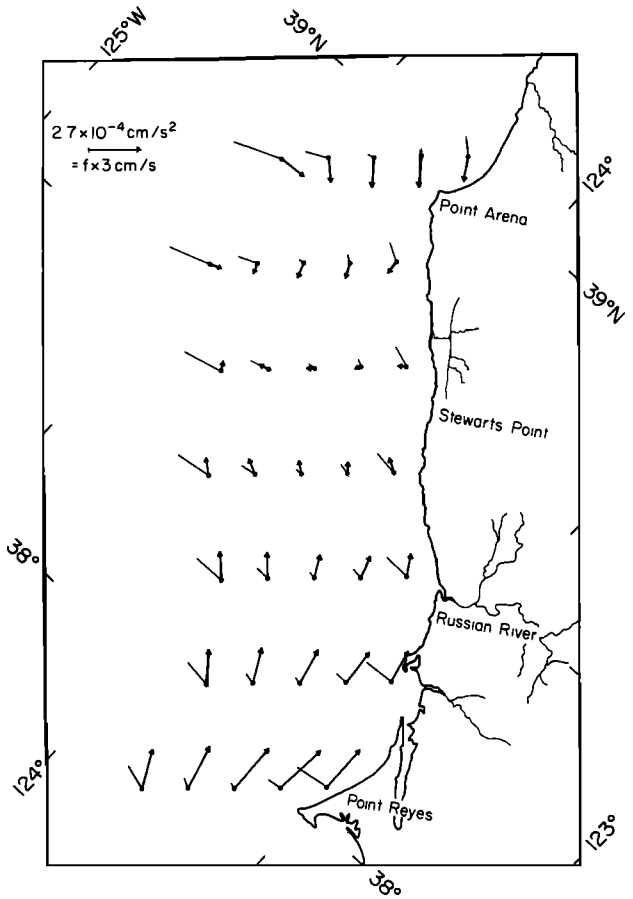

Fig. 15. The two eddy forcing terms driving the mean flow. The light arrows (without heads) are $\frac{1}{\rho}\mathbf{F}_H = \nabla \cdot \langle \mathbf{u}'\mathbf{u}' \rangle$, the effect of those eddy Reynolds stresses involving only horizontal flow. The dark arrows are the Lagrangian mean acceleration of surface drifters which, it is argued in the text, represents the net eddy forcing $\frac{1}{\rho}\mathbf{F}$ in the mean momentum equation (7). The mean flow driven by these terms is 90° to the left of the arrows.

change from zero at the coast to a value equal to that produced by an onshore wind stress of 1 dyne/cm^2 acting on a 10-m Ekman layer. This is unlikely because the measured mean across-shelf wind stress [*Mills and Beardsley*, 1982] at mid-shelf is about 0.3 dyne/cm^2 and directed offshore. It is more likely that the shear of $\langle v \rangle$ is associated with a change of surface slope of the order 10^{-6} across the inner shelf. Across-shelf sections of density taken near the C line of moorings by *Huyer* [1983] give no indication of rapid changes within 10 km of the coast, nor do the sections of geostrophic velocity computed from these by using *Reid and Mantyla*'s [1976] method of extrapolating bottom pressure over the shelf. It is, however, quite possible that there is a rapid decrease of across-shelf sea surface slope near the coast that is not accounted for by the extrapolation procedure.

The geostrophic balance in the across-shelf momentum equation does not explain why $\langle v \rangle$ is strongly sheared near the coast. It is tempting to explain this shear as a frictional effect associated with shallow water or proximity to the coast. In the alongshore component of (7) the (vertical, lateral) "frictional" terms are $(\partial_z \tau_y, \rho \partial_x \langle u'v' \rangle)$. It is plausible that near shore these terms dominate the alongshore momentum equation and that $\langle v \rangle$ adapts to bring them into near balance, much the way $\langle v \rangle$ adjusts to bring the surface and bottom stress into balance in a shallow viscous fluid acted on by the wind. Which frictional effect will dominate? From Figure 3 we see that $\partial_x \langle u'v' \rangle \approx -5 \times 10^{-5}$ cm/s^2 is an order of magnitude smaller than either the Coriolis acceleration $f\langle u \rangle$ inferred from Figure 2 or the $\frac{1}{\rho}\partial_z \tau_y$ that would be produced by the mean alongshore wind stress acting on a 35-m deep mixed layer. Thus the shear stress τ is the most likely cause of the small $\langle v \rangle$ found near the shore.

Using the mapping procedure in section 4.1, the contribution of horizontal mesoscale flow to the eddy Reynolds stress was computed from 1-day surface drifter velocities and the mean flow mapped in Figure 14. The divergence of this stress is shown in Figure 15 in the form of $\frac{1}{\rho}\mathbf{F}_H = \nabla \cdot \langle \mathbf{u}'\mathbf{u}' \rangle$. The forcing associated with the mean flow itself, i.e., $\nabla \cdot [\langle \mathbf{u} \rangle \langle \mathbf{u} \rangle]$, is smaller by a factor of 5 to 10. The structure of $\mathbf{F}_H$ is easily explained: the offshore component is essentially $\rho \partial_x \langle u'^2 \rangle$ and reflects the offshore gradient of across-shelf variability shown in Figure 2; the alongshore component of $\mathbf{F}_H$ is dominated by $\rho \partial_y \langle v'^2 \rangle$ and reflects the fact that both $\langle v'^2 \rangle$ and $\langle u'^2 \rangle$ increase by approximately a factor of 2 going from the south to the north in the region.

The magnitude of $\frac{1}{\rho}\mathbf{F}_H$ is of the order 10^{-4} cm/s^2 and thus has a dynamical effect comparable to a wind stress of 0.2 dyne/cm^2 acting on a 20-m-thick mixed layer. Thus lateral eddy stresses are not a dominant effect in upper-layer dynamics. However, if the stresses extend below the mixed layer (as the relatively gradual vertical variation of $\mathbf{u}'$ would suggest), $\mathbf{F}_H$ would be of significance in the lower-layer flow. In the steady state described by (7), $\mathbf{F}_H$ drives a downcoast flow (90° to the left of the arrows in Figure 15) that is convergent over the shelf and divergent over the slope. Because the ageostrophic flow driven by $\mathbf{F}$ is divergent, it may be more important than its size indicates.

One of the most remarkable drifter observations is that the mean velocity of drifters passing through a point varies as a function of time since passing through that point. Thus the pseudo-Lagrangian mean acceleration $\langle \frac{d}{dt}\mathbf{u} \rangle_L$ is not zero. Figure 15 shows the mean acceleration of surface drifters computed from the difference between successive velocities from the same drifter and averaged according to the central position. The pattern of Lagrangian acceleration is clear and not at all dependent on the method of mapping: drifters throughout the region accelerate toward a location somewhat south of Point Arena. As seen below, this acceleration provides a novel but interesting dynamical diagnostic.

Since surface drifters do not follow vertical water motion, the mean drifter acceleration is

$$\left\langle \frac{d}{dt}\mathbf{u} \right\rangle_L = \left\langle \frac{\partial}{\partial t}\mathbf{u} \right\rangle_E + \langle \mathbf{u} \cdot \nabla \mathbf{u} \rangle_E =$$

$$\nabla \cdot \langle \mathbf{u}\mathbf{u} \rangle_E - \langle \mathbf{u} \nabla \cdot \mathbf{u} \rangle_E \qquad (8)$$

The contribution of the mean velocity to terms on the right of (8) is smaller than the eddy contributions by a factor of 4–8. Thus the mean drifter acceleration is not an effect of the mean flow but rather a property of the eddy velocity $\mathbf{u}'$. An analogous phenomenon is seen in the Lagrangian mean velocity of particles in statistically steady turbulent flow in a pipe: particles identified near the pipe wall will have an average velocity that increases with time because a majority of them disperse toward the pipe center where the Eulerian mean velocity is greatest. In this case the Lagrangian mean acceleration is simply an indicator of the eddy momentum flux modeled by mixing length theory.

Because drifters are not true Lagrangian particles, interpretation of mean drifter acceleration is not straightforward and requires knowledge of the scale of the velocity components contributing to the terms on the right side of (8). If the vertical scales of $\mathbf{u}'$ are significantly greater than the depth h at which drifters follow the flow ($\approx$ 70 cm), then

$$-\langle \mathbf{u}'\nabla\cdot\mathbf{u}'\rangle = \langle \mathbf{u}'\partial_z w'\rangle =$$

$$\partial_z\langle \mathbf{u}'w'\rangle - \langle w'\partial_z\mathbf{u}'\rangle \approx \partial_z\langle \mathbf{u}'w'\rangle$$

since at the shallow depth h the vertical velocity is $O(h\nabla\cdot\mathbf{u})$ while $\partial_z\mathbf{u} \ll \mathbf{u}/h$ so that $w\partial_z\mathbf{u} \ll O(\mathbf{u}\nabla\cdot\mathbf{u})$. In this case

$$\rho\left\langle \frac{d}{dt}\mathbf{u}\right\rangle_L \approx \rho\nabla\cdot\langle \mathbf{u}'\mathbf{u}'\rangle_E + \rho\partial_z\langle w'\mathbf{u}'\rangle_E = \mathbf{F} \quad (9)$$

and drifter acceleration measures the total eddy forcing in the mean momentum budget (7). If, on the other hand, the scale assumption used in arriving at (9) is not valid, then no distinction can be drawn between the velocity components supporting τ and $\langle w'\mathbf{u}'\rangle$ and interpretation of drifter acceleration is indirect at best.

To the extent that (9) pertains, the results in Figure 15 indicate that eddy stresses tend to decelerate the downcoast flow in the northern region while accelerating it in the south. Thus the effect of $\mathbf{F}$ is similar to an upcoast (downwelling favorable) wind stress in the north and an upwelling favorable wind stress in the south. It can be seen in Figure 15 that the forcing by $\mathbf{F}$ is highly convergent with a relatively small curl. Thus in the steady state (7), the effect of $\mathbf{F}$ is to produce an upper layer velocity curl more than to modulate upwelling through $\nabla\cdot\langle\mathbf{u}\rangle$. While this forcing is small compared to $\partial_z\tau$, it may be more than coincidental that the structure of $\mathbf{F}$ is that required to cause the mean flow to follow the changing coastline orientation. Thus near Point Arena, $\mathbf{F}$ acts to deflect the downcoast mean to the east, while to the south the effect is a deflection to the west, just as is observed in Figure 14, and is required to follow the coastline and bathymetry.

5. Summary Discussion

As part of CODE a large number of inexpensive current-following near-surface drifters were used to explore the structure of coastal currents during the upwelling season. The descriptive results presented in part 1 show that the surface layer flow in the CODE region is often dominated by complex patterns that can be identified as fronts, eddies, jets and offshore "squirts." The most powerful offshore squirts were found at the coastal promontories Point Arena and Point Reyes, were more nearly recurrent transient features than permanent structures, and typically corresponded to features in the surface temperature field. In this paper the typical features of the CODE near-surface flow field are described, and the role of variability in establishing the mean state is examined. For discussion the velocity field is decomposed into an alongshore component v and across-shelf component, u, directed along the y and x directions, respectively. The velocities used for Eulerian averages, $\langle\cdot\rangle_E$, were computed from approximately 1-day displacements.

The offshore profile of $\langle v\rangle_E$ (Figure 2) shows a broad equatorward mean flow of the order 25 cm/s, with a strong shear zone ($\partial_x\langle v\rangle \approx 10\text{–}5\text{s}^{-1}$) in which $\langle v\rangle_E$ decreases near shore. There is significant mean offshore flow, which increases approximately linearly with offshore distance from near zero at the coast. The mean surface divergence ($\nabla\cdot\langle\mathbf{u}_H\rangle \approx 3\times 10^{-6}\text{s}^{-1}$) is uniformly distributed with offshore distance out to 40 km with no concentrated divergence near the shore. Without knowledge of surface layer depth it cannot be concluded if upwelling into the surface layer occurs across the shelf or if upwelling is localized near shore and velocity divergence is balanced by an offshore reduction of the thickness of a constant offshore transport layer. The two-dimensional map of surface velocity (Figure 14) discloses a significant alongshore divergence of $\langle v\rangle$ near Point Arena that leads to an "upwelling center" with surface divergence of the order $5\times 10^{-6}\text{s}^{-1}$.

In the surface layer heat budget of the entire CODE region the primary balance is between upwelling cooling and surface heating with onshore eddy heat flux playing a smaller role. In the Point Arena upwelling center, however, the cooling produced by $\partial_y\langle v\rangle$ can apparently be balanced only by a convergence of the alongshore eddy heat flux. In the absence of two-dimensional maps of near-surface temperature it is predicted that the required eddy heat flux convergence can be achieved only if the upwelling center is a local minimum of temperature.

Drifters are found to have a mean acceleration that (in section 4.3) is related to the total eddy forcing of the mean flow by eddy components bigger than about 1-m in scale; analogous accelerations are found in other turbulent shear flows. While this eddy forcing is not large enough to upset the approximate geostrophic balance of the alongshore flow, it appears to be important in the alongshore momentum budget. The eddy forcing disclosed by mean Lagrangian accelerations acts like an upcoast wind stress in the northern CODE region and like a downcoast stress in the southern region. This forcing steers the downcoast flow to the east passing Point Arena and to the west approaching Point Reyes, just as required to steer the flow along the changing bathymetry.

Maps of Eulerian averaged eddy Reynolds stress show that $\langle v'^2\rangle_E$ is largest at the coast, whereas $\langle u'^2\rangle_E$ increases offshore (Figure 3); approximate isotropy is achieved about 40 km offshore. The offshore variation of $\langle v'^2\rangle/\langle u'^2\rangle$ is a more or less inevitable consequence in nearly two-dimensional flow near a coast. Comparison of

Eulerian and Lagrangian time scales shows that the near-surface velocity variability in CODE is highly nonlinear in the sense that particle velocities are much faster than pattern propagation speeds (Figures 4 and 5). Near shore the Eulerian time scale of v exceeds that of u, but offshore the scales are comparable; the Lagrangian time scale of v always exceeds the analogous scale of u.

The eddy variability evident in the drifter trajectories in part 1 reduces the horizontal decorrelation scale of velocity to the order 40 km (Figure 6). The high correlation of currents at 1- and 30-m depth (Figure 6) indicates that the observed velocity variability is not superficial and suggests that eddy forcing may become even more important below the directly wind-driven layer. The alongshore scale of v exceeds that of u near shore, but like energy levels and time scales, the length scales of u and v are similar offshore (Figures 7 and 8). Despite the relatively short correlation scale of total velocity, 55% of the low-frequency near-surface kinetic energy can be described by a single mode with broad across-shelf variation and an alongshore wavelength of the order 200 km (Figure 9). This mode represents a coastally intensified alongshore flow coupled with an across-shelf flow that grows more or less linearly offshore from a small value near the coast; equatorward, v is associated with a diverging offshore u.

Some effects of eddy motion can be described by quasi-Lagrangian statistics of drifter motion. The mean transport of passive scalar properties is determined by the probability density of particle displacements. Drifter displacement statistics in CODE indicate that such transport is reasonably well modeled by eddy diffusion (Figure 11) with an anisotropic and inhomogeneous eddy diffusivity. After correcting for the effects of inhomogeneity and mean surface divergence, the diffusivity estimates in equation (4) were obtained. At an offshore distance of the order 10 km, $\kappa_{xx} \approx 10^6\,\mathrm{cm^2 s^{-1}}$ and $\kappa_{yy} \approx 3\times 10^7\,\mathrm{cm^2 s^{-1}}$; κ_{xx} increases offshore, while κ_{yy} decreases. These diffusivity estimates are the basis for the eddy heat flux estimates used in the upper-layer heat budget. While eddy diffusion may adequately characterize mean scalar transport, there seems no simple relation between lateral eddy fluxes of momentum and the mean shear. Use of κ as an eddy viscosity leads to variable errors of at least the order 10.

Particle-pair statistics describe stirring processes such as the dispersal of a scalar contaminant cloud. These processes cannot be modeled as diffusion in CODE, even if appeal is made to a scale-dependent diffusivity (Figure 12). Examination of particle separation probability densities suggests that the relative velocity between widely separated particles is approximately normally distributed. The relative velocity between closely spaced particles, however, is intermittent, perhaps because closely spaced particles can be trapped within the same small scale convergence.

Perhaps the greatest puzzle exposed by the CODE drifters is the origin or dynamical nature of the vigorous eddy variability found. There are three general categories of phenomena that might contribute to this variability: (1) coastally trapped topographic waves generated by the wind; (2) offshore eddy motion impinging on the coast; and (3) eddies generated by irregular coastal bathymetry.

The most wavelike feature found is the dominant empirical mode found from the covariance of 3-day low-passed velocities. This mode appears to have a characteristic wavelength of the order 200 km and, from Eulerian current measurements it might be supposed, a period of the order 5 days. The structure is that of a coastally intensified alongshore flow coupled with strong across-shelf flow that is highly divergent. *Clarke and Brink* [1984] have recently computed the structure of wind forced topographically trapped waves in conditions characteristic of the CODE region. Their calculations show an alongshore current structure similar to that of the observed mode. The predicted propagation velocity is, however, significantly greater than can be rationalized with the empirical mode's space and time scales. Further, it seems unlikely that any parameter tuning in the model could reproduce the strong observed across-shelf velocity in a wave capable of propagating significant distances (recall that our observations indicate that the observed velocity variability is not superficial).

The strong nonlinearity and vigorous offshore flow associated with squirts found here argues that much of the CODE velocity variability has more in common with mesoscale eddies than with quasi-linear propagating waves. The complex surface temperature patterns, which generally correspond to drifter tracks, are not often seen to propagate significantly, and when detectable, the sense of propagation is to the south. For example, of the drifter patterns shown in part 1, several (Figures 5, 7, 9, 12, and 13) correspond to persistent surface temperature patterns that more nearly evolve and distort than they propagate; one example (Figure 8) corresponds to a highly coherent cold-core eddy that propagates slowly (2—4 cm/s) to the south. The minimal observed propagation speeds also suggest that the near-surface velocity field is more like a field of eddies than waves. From the descriptive picture in part 1 the most wavelike occurrences seem to be the current reversals that follow wind relaxations and appear to propagate poleward.

In summary we have used a large number of current-following drifters to examine a particular coastal region during the upwelling season. Both descriptive and statistical views show the flow to be vastly more complex than imagined in models of wind-forced coastally trapped waves or of broad scale upwelling forced by Ekman transport. It is to be hoped that, as the analysis of the total CODE data set matures, the nature of the dynamical processes involved will clarify.

APPENDIX. THE COVARIANCE OF FILTERED VELOCITY

Let the filtered velocity be defined

$$\tilde{\mathbf{u}}(\xi,y,t) = \int d\tau\, d\eta\, d\zeta\, h(\xi-\zeta, y-\eta, t-\tau)\mathbf{u}(\zeta,\eta,\tau)$$

where h is a rectangular function of unit volume centered at the origin with widths $\Delta\xi = 10$ km, $\Delta y = 20$ km, and $\Delta t = 3$ days. Assuming stationarity and alongshore homogeneity, the covariance of unfiltered velocity is

$$C(\xi_1,\xi_2,y,t) = \langle \mathbf{u}'(\xi_1,y_o,t_o)\mathbf{u}'(\xi_2,y_o+y,t_o+t)\rangle ,$$

where averaging is over all values of y_o and t_o. The covariance of the filtered signal is

$$\bar{C}(\xi_1,\xi_2,y) = \int d\eta \int d\tau \int d\zeta_1 \int d\zeta_2 \; W(\xi_1-\zeta_1,\xi_2-\zeta_2,y-\eta,\tau)\, C(\zeta_1,\zeta_2,\eta,\tau) \;, \quad \text{(A1)}$$

where

$$W(\xi_1,\xi_2,y,t) = \int d\eta \; d\tau \; h(\xi_1,y-\eta,t-\tau)h(\xi_2,\eta,\tau) \;,$$

also has unit volume.

The filtered velocity covariance (A1) was estimated as

$$\bar{C}(\xi_1,\xi_2,y) = \frac{\sum_n W_n \; \mathbf{u}'(\zeta_{1n},y_n,t_n)\mathbf{u}'(\zeta_{2n},y_n+\eta_n,t_n+\tau_n)}{\sum_n W_n} \;,$$

where

$$W_n = W(\xi_1-\zeta_{1n},\xi_2-\zeta_{2n},y-\eta_n,\tau_n) \;,$$

and the sum over n includes the positions ξ_{1n},y_n,t_n and $\xi_{2n},y_n+\eta_n,t_n+\tau_n$ of all velocity observation pairs. This form amounts to a finite difference approximation to (A1) in which the integrand is weighted by the number of observations going into the sample average of the unfiltered covariance $C(\zeta_1,\zeta_2,\eta_n,\tau_n)$.

Acknowledgments. Lloyd Regier, Jim Dufour, and Gerald Parks were responsible for the operational success of this project. Jane Huyer and Mike Kosro shared responsibility for deploying the drifters. This work was supported by the National Science Foundation under grant OCE80-14942.

REFERENCES

Batchelor, G. K., Diffusion in a field of homogeneous turbulence, 2, The relative motion of particles, *Proc. Cambridge Phil. Soc., 48*, 345—362, 1952.

Bretherton, F. P., R. E. Davis, and C. B. Fandry, A technique for objective analysis and design of oceanographic experiments applied to MODE-73, *Deep-Sea Res., 23*, 559—582, 1976.

Bryden, H. L., D. Halpern, and R. D. Pillsbury, Importance of eddy heat flux in a heat budget for Oregon coastal waters, *J. Geophys. Res., 85*, 6649—6653, 1980.

Clarke, A. J., and K. H. Brink, The response of stratified, frictional shelf and slope waters to fluctuating large-scale low frequency wind forcing, unpublished, 1984.

Csanady, G. T., *Turbulent Diffusion in the Environment*, 248 pp., D. Reidel, Hingham, Mass., 1973.

Davis, R. E., On relating Eulerian and Lagrangian velocity statistics: Single particles in homogeneous flows, *J. Fluid Mech., 114*, 1—26, 1982.

Davis, R. E., Oceanic property transport, Lagrangian particle statistics, and their prediction, *J. Mar. Res., 41*, 163—194, 1983.

Davis, R. E., Drifter observations of coastal surface currents during CODE: The descriptive view, *J. Geophys. Res.*, this issue.

Davis, R. E., 1985, Objective mapping by least squares fitting, *J. Geophys. Res.*, in press.

Freeland, H. J., P. B. Rhines, and T. Rossby, Statistical observations of trajectories of neutrally buoyant floats in the North Atlantic, *J. Mar. Res., 33*, 383—404, 1975.

Garrett, C., On the initial streakiness of a dispersing tracer in two- and three-dimensional turbulence, *Dyn. Atmos. Oceans, 7*, 265—277, 1983.

Huyer, A., Hydrographic observations along the CODE central line off Northern California, 1981, *J. Phys. Oceanogr.*, in press, 1984.

Kenyon, K. E., Stokes drift for gravity waves, *J. Geophys. Res., 74*, 6991—6994, 1969.

Mills, C. A., and R. C. Beardsley, CODE-1: Coastal and moored meteorological observations, CODE-1 Moored Data Report, *Tech. Rep. 82-23*, pp. 17—54, Woods Hole Oceanogr. Inst., Woods Hole, Mass., 1983.

Mooers, C. N. K., C. A. Collins, and R. L. Smith, The dynamic structure of the frontal zone in the coastal upwelling region off Oregon, *J. Phys. Oceanogr., 6*, 3—21, 1976.

Nelson, C. S., Wind stress and wind stress curl over the California Current, *Tech. Rep. NMFS SSRF-14*, 87 pp., Nat. Oceanic Atmos. Admin., Washington, D.C., 1977.

Reid, J. L., and A. W. Mantyla, The effect of geostrophic flow upon coastal sea elevations in the northern North Pacific, *J. Geophys. Res., 81*, 3100—3110, 1976.

Richardson, L. F., Atmospheric diffusion on a distance-neighbor graph, *Proc. R. Soc. A., 110*, 709—737, 1926.

Richman, J., and A. Badan-Dangon, Mean heat and momentum budgets during upwelling for the coastal waters off Northwest Africa, *J. Geophys. Res., 88*, 2626—2632, 1983.

Winant, C .D., and A. W. Bratkovich, CODE-l: Moored current observations, CODE-1 Moored Data Report, *Tech. Rep. 82-83*, edited by L.K. Rosenfeld, pp. 55—80, Woods Hole Oceanogr. Ins., Woods Hole, Mass., 1983.

R. E. Davis, Scripps Institution of Oceanography, University of California at San Diego, Mail Code A-030, La Jolla, CA 92093.

(Received May 22, 1984;
accepted July 16, 1984.)